Zhang Ding (Orcid ID: 0000-0002-3501-5486)

[4664]-1
Received: 23 July 2018 | Accepted 7 May 2019

Running head: ZHANG ET AL.

ARTICLE

Simulated and experimental estimates of hydrodynamic drag from bio-logging tags

Ding Zhang[1] | Julie M. van der Hoop[2,3,4] | Victor Petrov[5] | Julie Rocho-Levine[6] | Michael J. Moore[2] | K. Alex Shorter[1]

[1]University of Michigan, Ann Arbor, Michigan

[2]Massachusetts Institute of Technology-Woods Hole Oceanographic Institution Joint Program in Oceanography/Applied Ocean Science and Engineering, Massachusetts

[3]Woods Hole Oceanographic Institution, Woods Hole, Massachusetts

[4]Aarhus University, Institute for Bioscience, 8000 Aarhus C, Denmark

[5]University of Michigan, Ann Arbor, Michigan

[6]Dolphin Quest Oahu, Honolulu, Hawaii

Correspondence

K. Alex Shorter, 3534 George G. Brown Laboratory, 2350 Hayward

Ann Arbor, MI 48109-2125

Email: kshorter@umich.edu

ABSTRACT

Drag force acting on swimming marine mammals is difficult to measure directly. Researchers often use simple modeling and kinematic measurements from animals, or computational fluid dynamics (CFD) simulations to estimate drag. However, studies that compare these methods are lacking. Here, computational simulation and physical experiments were used to estimate drag forces on gliding bottlenose dolphins (*Tursiops truncatus*). To facilitate comparison, variable drag loading (*no-tag, tag, tag+4, tag+8*) was used to increase force in both simulations and experiments. During the experiments, two dolphins were trained to perform controlled glides with variable loading. CFD simulations of dolphin/tag geometry in steady flow (1–6 m/s) were used to model drag forces. We expect both techniques will capture relative changes created by experimental conditions, but absolute forces predicted by the methods will differ. CFD estimates were within a calculated 90% confidence interval of the experimental results for all but the

tag condition. Relative drag increase predicted by the simulation vs. experiment, respectively, differed by between 21% and 31%: *tag*, 4% vs. 33%; *tag+4*, 47% vs. 68%; and *tag+8*, 108% vs. 77%. The results from this work provide a direct comparison of computational and experimental estimates of drag, and provide a framework to quantify uncertainty.

KEYWORDS

bio-logging, computational fluid dynamics, CFD, drag, tag

1 | INTRODUCTION

Animal-borne sensors provide information that enable researchers to measure, visualize, and quantify how and why animals move and interact with their environment (Gabaldon, Zhang, Barton, & Johnson-Roberson, 2017; Hussey et al., 2015; Johnson, Tyack, Nowacek, & Shorter, 2000; Kays, Crofoot, Jetz, & Wikelski, 2015; Wilson, Shepard, & Liebsch, 2008; Zhang et al. 2018, 2019). The rise of mobile computing has resulted in technological improvements that have decreased size, improved power efficiency and reduced cost of the electronics and sensors used to create bio-logging tags. As a result, tag designs have diversified and become more available to researchers in the community; as such, we have seen a tripling of permit applications to tag animals (Jones et al., 2013), as well as major increases in the number and diversity of subject species and the number of tags deployed on animals (Hussey et al., 2015; McIntyre, 2014).

In the marine environment, placing tags on a highly streamlined body has the

potential to affect swimming mechanics by increasing drag on the body. During swimming, thrust output required to overcome drag is central to energetic expenditure; quantifying forces acting on the body when swimming with tags is essential to determine the potential for and magnitude of tag effects on energy consumption or swimming behavior (e.g., van der Hoop et al. 2014, 2018). Direct measurement of propulsive forces during swimming is difficult, but estimates of drag loading and direct measurement of the animal's specific acceleration can be used to estimate propulsive force (López, de Soto, Miller, & Johnson, 2016; Ware, Trites, Rosen, & Potvin, 2016).

Glide deceleration (Bilo & Nachtigall, 1980; Lang & Daybell, 1969) has been widely used to estimate passive drag coefficients from free-swimming animals. During a glide of a neutrally buoyant animal, a net drag force opposes the movement of the body, slowing it down. A measured rate of deceleration can then be used to calculate drag force (Bilo & Nachtigall, 1980; Lang & Daybell, 1963). Along with glide deceleration, wind tunnels with

physical models (Hanson, 2001; Jones et al., 2013) and tow experiments with live animals in a rigid body position (Feldkamp, 1987) have been used to measure static drag coefficients.

Data from bio-logging tags (Aoki et al., 2011; Miller et al., 2004; Ware et al., 2016), along with estimated body parameters, have been used to estimate drag forces on free-swimming animals. While methods using glide data are only useful for models that describe or quantify gliding behaviors, they still provide a baseline for relative comparison of different drag conditions, *e.g.*, with instrumentation (Skrovan, Williams, Berry, Moore, & Davis, 1999) or during and after pregnancy (Noren, Redfern, & Edwards, 2011). However, measurements made from animal-borne sensors are often required for these estimates, leaving the additional contribution created by the tag difficult to discern.

To complement measurements of static drag coefficients, researchers have performed controlled experiments with managed animals trained to execute prescribed swimming tasks

to estimate drag forces and coefficients (Noren et al., 2011). The use of a controlled experimental environment allows data collection during uninstrumented trials, enabling the quantification of a tag's contribution to the net drag acting on the combined system. In contrast with the experimental methods described above, computational fluid dynamics (CFD) models are becoming an increasingly popular method to simulate the expected effects of instrumentation and to refine tag design (Balmer et al., 2014; Hazekamp, Mayer, & Osinga, 2010; Pavlov & Rashad, 2012; Shorter, Murray, Johnson, Moore, & Howle, 2014; van der Hoop et al. 2014, 2018). The same technique has also been used to aid and optimize the design of underwater vehicles (Joung, Sammut, He, & Lee, 2012; Phillips, Turnock, & Furlong, 2010; Shereena, Vengadesan, Idichandy, & Bhattacharyya, 2013). Working in a simulated environment enables a rapid evaluation of a range of tag designs in multiple fluid-flow conditions, but these simulations can be difficult to compare with experimental results.

In this work, we investigate two questions: (1) How do experimentally measured drag forces compare to numerical simulation results? (2) How much does a bio-logging tag increase the net drag force acting on a bottlenose dolphin during a controlled gliding task? To investigate these questions, we use CFD simulations and experimental measurements of gliding bottlenose dolphins (*Tursiops truncatus*) to (1) assess and compare estimated drag force calculated using simulated and experimental data and (2) investigate the relative load created by tags of different sizes. We expect that (1) smaller tags will create less additional drag, (2) the relative increase in drag created by the tags in both simulation and experiment will be comparable, but (3) the absolute force predicted by methods will differ. The results from this work improve our ability to interpret estimates of drag force derived from CFD simulations, and provide a framework to quantify the uncertainty of experimentally driven estimates of drag. All symbols and abbreviations used in this work are listed in Table 1.

2 | METHODS

2.1 | Experimental setup

To experimentally investigate the effects of tag drag, we fabricated a modular set of elements to increase frontal area by up to eight times the tag alone (Figure 1). Two male bottlenose dolphins at Dolphin Quest Oahu were trained to glide with no locomotory movement on cue between marine mammal specialists standing or floating in water 8–12 m apart (Figure 1). One specialist provided the initial propulsive force before releasing the animal to glide to the second specialist. Dots of zinc oxide on the dolphin's skin were used to create kinematic markers visible in underwater video footage, and were used to calculate the position and speed of the animal during the trial. Glides were filmed perpendicular to the path of the animal at 30 fps with a Canon PowerShot G12 digital camera in a waterproof housing (Canon WP-DC34). The distance between the markers was measured following the application to each subject. The camera and housing were mounted

on a monopod, which was rested on the bottom of the lagoon to reduce the camera's motion from water movement. The experimental lagoon was 1.5–2.4 m deep. The dolphins were asked to perform glides without the tag (control), wearing a *tag*, and wearing the tag with either four (*tag+4*) or eight (*tag+8*) drag elements (Figure 1). Each drag element had the same cross-sectional area as the tag itself. The *tag+4* configuration increased the cross-sectional area by four while the *tag+8* configuration increased it by eight.

2.2 | Identification of successful trials for analysis

We used the following criteria to select glides for analysis: (1) no visible body movement, (2) no visible changes in the horizontal plane (i.e., the dolphin did not noticeably move closer to or away from the camera), (3) minimal changes in depth, (4) 1 s minimum glide duration, and (5) a change in acceleration < 0 (i.e., there was a detectable decrease in speed) (Noren et al. 2011; Stelle, Blake, & Trites, 2000). Glide duration was calculated from the time the kinematic markers entered the frame to when the

dolphins showed detectable body movement. We calculated success rates based on the number of glides the dolphins were asked to perform and the number of glides that were successful for each individual and each tag condition.

2.3 | Video processing

All video processing was conducted in MATLAB and made use of the *PointTracker* object from the *Computer Vision System Toolbox*. An example video frame of a gliding dolphin with kinematic markers (zinc oxide) is shown in Figure 2. Videos were first preprocessed using the MATLAB *Image Processing Toolbox* to enhance marker visibility. Each frame was converted into gray scale and then object edges were identified using the *edge* function. Invalid small objects/edges were removed using the *bwareaopen* function, and the *imclose* function was used to close edges in each frame morphologically. Finally, the original frames were overplayed with the resulting binary frames to obtain the preprocessed video.

A semiautomatic tracking program was developed to extract kinematic marker positions

from the enhanced video. Features around the kinematic markers were first identified in each frame (Figure 2c). Marker position during the trial was then estimated by averaging tracked feature positions. In most cases, feature identification was automatic; however, when the number of tracked features per marker dropped below two, a human analyst was queried to identify marker position in the frame.

In this work, the known distance between the two kinematic markers was used to correct for lens distortion and to map dolphin speed from video to world frame. Figure 2d shows an example of the pincushion distortion created by the camera lens/housing that was as large as five pixels at the frame edge. To correct the error, a third-order polynomial was fit to the distorted distance data (Figure 2d, red line). The functional fit was used to undistort position data around the center of the frame. Speed was then calculated by numerically differentiating position data and mapped to the real world using the following relationship:

$$U = \frac{d_w}{d_v} U_v \quad (1)$$

where U and U_v are speeds of dolphin in real world and in the video, d_w and d_v are distance between kinematic markers in real world and in video respectively.

2.4 | Dynamic model of the glide

Drag force (F_d),

$$F_d = 0.5 \rho U^2 A_w C_d \quad (2)$$

was modeled as a function of water density (ρ), the relative speed of the animal in the water (U), the drag coefficient of the animal (C_d), and the wetted surface area of the animal (A_w), which was calculated from the mass of the animal and the empirical relationship presented in Fish (1993). All experimental data were collected within 2–2.6 body diameters of the surface, and are subject to additional drag force created by dynamic interactions with the surface (Hertel 1966). The average depth of each animal

over all the experimental trials was used to determine the value of γ based on Hertel (1966). We use $C_{d\_correct}$ to denote the drag coefficient that has been corrected for additional surface drag, and used it to compare with results from CFD and the literature.

$$C_{d\_correct} = C_d/\gamma \quad (3)$$

In this experiment, the dolphins were gliding horizontally without active locomotion. As such, we assume (1) the animal can be treated as a single rigid body, (2) deceleration occurs only in the surge direction, and (3) the net drag force is the only external force acting on the body. The net drag force can then be related to the acceleration of the body:

$$\sum F = F_d = m_b a_b \quad (4)$$

where m_b is the induced (virtual) mass of the dolphin (Vogel 1994) and a_b is the specific acceleration of the center of mass. The induced mass was calculated as follows:

$$m_b = m + C_a \rho V \quad (5)$$

where m is the mass of the animal C_a is the added mass coefficient and V is the volume of the animal estimated from the model used for the CFD simulations. The differential equation modeling the speed of the animal during the glide can be expressed as,

$$\frac{F_d}{m_b} = a_b = -\frac{dU}{dt} = \frac{U^2 \rho A_w C_d}{2m_b} \quad (6)$$

The negative sign indicates that the direction between acceleration and speed are opposite. Solving (Equation 6) results in an explicit relationship between speed and time:

(7)

$$U(t) = \frac{1}{\left[\left(\frac{\rho A_w C_d t}{2m_b}\right) + \left(\frac{1}{U_0}\right)\right]}$$

where U_0 is the initial speed at the start of the trial. In Equation 7, ρ, A_w, and m_b are constant parameters describing the animal or the environment, and $U(t)$ is dependent on the drag coefficient and the initial velocity of the animal. Kinematic information extracted from the experimental video data and a curve-fitting optimization approach were used to determine the drag coefficients for the animals using the model and the experimental data.

2.5 | Parameter optimization

A dual parameter sweep was performed to identify the initial speed (U_0) and the coefficient of drag (C_d) for the model that best matched the experimental results. U_0 was considered unknown because it was a critical parameter for the curve-fitting process and

the noise in the extracted speed data made it difficult to estimate U_0 directly. For the sweep, the initial speed (U_0) ranged from 0 to 1.5 m/s with an interval step of 0.01 while the coefficient of drag (C_d) ranged from 0 to 0.3 with an interval step of 0.0005. These parameter ranges were based on published values in the literature (Fish, 1998; Fish, Legac, Williams, & Wei, 2014; Noren et al., 2011). Each combination of U_0 and C_d yields a predicted speed curve according to Equation 7; the fit quality of the curve was quantified using the RMS (root mean square) value of the residual, R, between measured speed and predicted speed. A surface, called the R-surface (Figure 3, top row), in 3D space was then formed by combining all pairs of (U_0, C_d) and the resulting R. Given that a smaller R value indicates a better fit, the values of U_0 and C_d located at the global minima of the R-surface were selected for the final models.

When multiple qualified trials (each indexed by k) were obtained for an experimental condition, speed data were pooled to estimate the drag coefficient. A similar

optimization approach was used to identify the best fit from *N* coefficient candidates. The goodness of each drag coefficient candidate $C_d^{(n)}$ was evaluated individually. The constant $C_d^{(n)}$ was applied for the *k*-th trial, together with a varying initial speed (U_0), to find the corresponding lowest cost $R_{(k)}^{(n)}$ for the *k*-th trial. In other words, $R_{(k)}^{(n)}$ is the smallest residual that can be obtained by varying only initial speed (U_0) for the *k*-th trial and *n*-th drag coefficient. The overall cost of all *K* trials corresponds to the *n*-th drag coefficient $C_d^{(n)}$ is defined as:

$$R_{\text{all}}^{(n)} = \sum_{k=1}^{K} R_{(k)}^{(n)} \tag{8}$$

where small values of $R_{\text{all}}^{(n)}$ indicate values of $C_d^{(n)}$ that result in a good fit. The $C_d^{(n)}$ with the lowest residual, among all *N* drag coefficient candidates (i.e., $C_d^{(1)}$ … $C_d^{(N)}$), was then

selected for the model. The resulting drag coefficient is denoted as C_{d_all}:

$$C_{d\_all} = C_d^{(n)} \quad s.t. \quad n = \arg\min R_{all}^{(n)} \tag{9}$$

The average drag force acting on the animal could then be calculated using Equation 2, where U corresponds to the average speed during a particular trial. The percent increase in drag coefficient between the tagged conditions and the nontagged animal was calculated for both the experimental and simulation results:

$$\left[\frac{(C_{d\_tagged} - C_{d\_notag}}{C_{d\_notag}}\right] * 100 \tag{10}$$

This provides a reference of the increase in a nondimensional quantity for comparison of tag effects (Jones et al. 2013). We also calculated the Reynolds number (Re) to compare drag coefficients within this study and to other values in the literature:

$$\mathrm{R}e = \frac{lU_0}{v} \quad (11)$$

where l is the body length (in meters; Table 2), U_0 the speed at the start of the glide (meters/second) and v the kinematic viscosity of seawater (1.05×10^{-6} m^2/s).

2.6 | Computational fluid dynamics (CFD)

Building on previous work (Shorter et al. 2014), CFD simulations were performed using CAD (computer-aided design) models of the tag and drag elements with representative animal geometry. Autodesk Inventor 2013 (Autodesk Inc., San Rafael, CA) was used to model the tag geometry, and dolphin geometry was scaled to match the average length of the animals in the experimental trials (2.48 m) at Dolphin Quest Oahu (Honolulu, HI).

Simulations were performed using STAR-CCM+ (version 9.04; CD-adapco, Melville, NY). This commercial code solves the transport equations for continuity and 3-D momentum on a very fine 3-D mesh. We modeled turbulence with the two-layer Reynolds-averaged Navier-Stokes (RANS) approach for the solution of the k-ε transport equations (STAR-CCM+; Rodi,

1991). Mesh sensitivity tests were performed in 2D with a dolphin middle cross-section profile to estimate required cell size. We tested three different mesh sizes (coarse = 0.05 m, medium = 0.025 m, and fine = 0.01 m) with 0.365 million, 0.998 million, and 6.50 million cells, respectively. Variation in drag and lift forces from medium to fine mesh was 1.85%. The 3D simulations were performed with trimmed cell mesh (0.25 m cell base size) with 50–57 million cells; the number of cells depends on the tag configuration with more drag elements requiring more cells. The 3D computation domain has a cylindrical shape with a length of 10.4 m and diameter of 6 m (Figure 4). The modeled dolphin length is 2.6 m with a body diameter approximately 0.2 m at the dorsal fin. During all simulations of the combined dolphin-tag model, the tag was located 0.74 m from the rostrum midway between the blow hole and dorsal fin. Simulations were constructed with a uniform velocity profile over a range of speeds (1–6 m/s). Maximum collection blockage area is below 0.6% with the object to the domain volume ratio of 0.4%. Boundary

conditions were applied as (1) uniform velocity at the inlet, (2) outflow boundary (zero normal gradients) at the outlet, and (3) slip wall around the domain.

For all simulations, a polynomial function was used to interpolate forces at flow speeds between simulated points. Drag coefficients (C_{d_sim}) were calculated for each condition using:

$$C_{d\_sim} = \frac{\sum_f \left(F_f^{pressure} + F_f^{shear}\right) \cdot n_D}{\frac{1}{2}\rho_{ref} v_{ref}^2 a_{ref}} \quad (12)$$

where $F_f^{pressure}$ and F_f^{shear} are the pressure and shear force vectors on the surface face f and ρ_{ref}, v_{ref}, and a_{ref} are the reference density, velocity, and area, respectively. n_D is a user-specified direction vector. The pressure force vector on the surface was computed as:

$$F_f^{pressure} = (p_f - p_{ref}) a_f \quad (13)$$

where p_f is the face static pressure, a_f is the face area vector, and p_{ref} is the reference pressure. Shear force is also exerted on the surface face f by the moving fluid and was computed as:

$$F_f^{shear} = T_f \cdot a_f \quad (14)$$

where T_f is the stress tensor at face f. The achieved level of residual convergence for all equations was below 1×10^{-6}. Additional simulations were performed to confirm that simulation results were independent of upstream and downstream domain lengths.

2.7 | Statistical analysis

Bootstrapping was used to create a confidence interval for the drag coefficients derived from the experimental data (DiCiccio & Efron, 1996). All experimental data for a given trial/animal was treated as a complete population. A simulated data set, with each

condition trial containing the same number of data points as the original data set, was created by sampling with replacement. Regression and parameter estimation from the simulated data were performed in the same manner as described above to obtain an estimated drag coefficient, $\hat{C}_d^{(b)}$. This was repeated B times (B = 500) to obtain a set of estimates ($\hat{C}_d^{(1)}$, $\hat{C}_d^{(2)}$, … $\hat{C}_d^{(B)}$), which were used to obtain a 90% confidence interval (CI) for the experimentally derived drag coefficient.

A two-way ANOVA with post hoc Tukey's HSD was used to test whether drag coefficients from CFD simulations were significantly different between tag conditions (*no tag*, *tag*, *tag+4* and *tag+8*), while considering the effect of velocity. We used ANOVA with post hoc Tukey's HSD to test for the effects of drag loading and individual on (1) drag coefficients estimated from experimental data and (2) glide duration.

3 | RESULTS

A total of 27 glides fit the necessary criteria for analysis (Table 2). Speed data for the model optimization were calculated from undistorted displacement data (Figure 2d). Representative speed data from a glide, results from the parametric optimization and an example of the resampled model fit used in the bootstrapping analysis are presented in Figure 3. In the example, the parameters that minimized the fit residual to the speed data were C_d = *0.0265* and U_0 = 0.78 (Figure 3, middle). The parameters that fit the resampled data were $\hat{C}_d = 0.0290$ and $\hat{U}_0 = 0.79$ (Figure 3, bottom).

The uncorrected drag coefficients for the full data optimizations (C_{d_all}) ranged from 0.011 to 0.028, with the identified initial velocities ranging from 0.5 to 1.07 m/s (Table 3, Figure 5). Fit residuals for the full data optimization ranged from 0.12 for the *tag* to 0.21 for the *tag+8* condition for the two animals. There was a significant effect of tag condition on the estimated drag coefficients (ANOVA; $F_{3,22}$ = 7.5318, p = .0012); we detected no significant effect of individual ($F_{1,22}$ = 0.6934, p = .4139). There

was no detectable increase between animals when not instrumented and when wearing the tag alone (post hoc Tukey's; p = .7505). The *tag+4* significantly increased C_d, by 126.4% (p = .0019) and the *tag+8* by 192.5% (p = .0013) compared to when the dolphins were not instrumented. From the experimental data, the *tag+4* and *tag+8* did not lead to significantly greater C_d compared to the *tag-only* (p = .1557 and .1664, respectively). The surface-induced drag corrected coefficients ($C_{d\_all\_correct}$) are also reported in Table 3, and are comparable to the simulated results.

The glide durations lasted on average 2.1 s (± 0.75 SD) and, with the exception of TT01's single trial during the *tag* condition, were relatively consistent. We detected no significant effect of tag condition on glide duration ($F_{3,22}$ = 1.2501, p = .3157). Success rates varied between the different conditions and individuals, with dolphin TT01 not able to successfully complete a glide with all the drag elements (*tag+8*; Table 2).

Qualitatively, CFD simulations show the flow disturbance during the loading

conditions (Figure 6). The *tag* condition creates a minor disturbance to the flow, forming a small region of recirculation upstream of the dorsal fin. Additional drag elements (*tag+4* and *tag+8*) significantly increased the recirculation region, which eventually occupies the entire space between the tag and the dorsal fin. This effect is also visible downstream from the dolphin body. The flow redistribution was reflected in the increased magnitude of the force acting on the coupled system.

Drag coefficients calculated from the CFD simulations increased as more elements were added (*tag+4* and *tag+8*), and ranged from 0.0071 to 0.0207. These results were comparable to the corrected experimental coefficients, with all but the CFD *tag* condition within a calculated 90% confidence interval of the experimental results. In the region near the tag, the velocity of the fluid increased as it moved over the top of the body creating an area of low-pressure behind the tag. These flow disturbances increased drag forces on the dolphin body (Figure 7 top). As speed increased from 1 to 6 m/s, drag

forces on the animal model increased from 15 N to 387 N (Table 4). The *tag* added 1–25 N across these speeds, increasing the drag coefficient by only 4% from 0.0076 to 0.0080. There were significant effects of flow speed (two-way ANOVA; $F_{1,24}$ = 70.3, p < .0001) and tag condition ($F_{4,24}$ = 541.3, p < .0001) on CFD-derived drag coefficients. The addition of the tag did not yield a significant increase in drag coefficient (post hoc Tukey's; p = .6119). In contrast, the *tag+4* and *tag+8* conditions increased the drag coefficient by 67% and 152%, respectively, compared to the noninstrumented condition (Table 4; p < .0001 for both comparisons). Additionally, drag coefficients for the *tag+4* and *tag+8* were significantly higher than the *tag* alone (p < .0001 for both comparisons).

To compare the experimental and simulation results directly, drag force acting on TT02 in 1 m/s flow were calculated for all tag conditions using (1) the experimentally derived drag coefficient (C_{d_all}); (2) the corrected experimental coefficients ($C_{d\_all\_correct}$); and (3) simulated coefficients (C_{d_sim}), Figure 7 bottom. The 90% confidence

intervals for each of the experimental force estimates are presented to capture uncertainty in the estimates. The magnitude of the simulated force estimates was smaller than the forces predicted using the experimental results. The relative increase in drag force created by the tag conditions varied between the two estimates, with the relative increase predicted by the experiment larger for the *tag* condition (4% vs. 33%), comparable for the *tag+4* (47% vs. 68%), and smaller (108% *vs*. 77%) for the *tag+8*.

4 | DISCUSSION

The ability to estimate drag force from a swimming animal is key to an improved understanding of how bio-logging tags may impact animal behavior and energetic cost. To this end, we modified drag on gliding bottlenose dolphins with a modular tag system, collected experimental data that were used to estimate drag, and compared those experimental estimates to results from CFD. The simulations and experiments complement each other in this work, with the physical experiments providing data to verify the

simulations, and the virtual model extending the study to conditions that are hard to achieve experimentally.

The free-stream speeds used in simulation (1–6 m/s; ~0.4–2.5 *l*/s, Reynolds numbers between 2×10^6 and 1×10^7) reflect the natural range of swimming speeds in dolphin species. Although dolphins are known to have a high capacity for maximum swimming speeds when trained (6.5–8.2 m/s; 2.5–3.8 *l*/s) (Rohr, Latz, Fallon, Nauen, & Hendricks, 2002) or when performing burst behaviors (15 m/s; 5.9 *l*/s) (Lockyer & Morris, 1987), routine speeds are much lower (1.6–5.6 m/s; 0.6–2.2 *l*/s) (Irvine, Wells, & Scott, 1982; Mate et al., 1995; Shane, 1990; Ridolix et al., 1997; Würsig & Würsig, 1979). Minimum transport costs (COT_{min}) occur at swimming speeds of 2.1–2.5 m/s (~1 *l*/s) (Williams, Friedl, & Haun, 1993; Yazdi, Kilian, & Culik, 1999). CFD simulations enabled a virtual representation of the dolphin-tag system, and the resulting flow visualization provided a qualitative means of assessing the impact of tag geometry on the flow field around the animal (Figure 6)

(Shorter et al., 2014).

Transition from laminar to turbulent flow occurs somewhere between 5×10^5 and 1×10^7, depending on the shape and smoothness of the body (Vogel, 1994). During a glide, velocity increases at the rostrum and along the front of the body in areas of high pressure, maintaining a thin boundary layer with low viscous forces (Figure 6) (Ungerechts, Daly, & Zhu, 1998). Velocity and pressure decrease as flow passes the widest point of the body, 0.34–0.45 l (Fish, 1993); the transition to turbulent flow is most likely to occur at this point (Lighthill, 1971). Pressure-drag increases due to the imbalance of pressure in front of and behind this widest point (Ungerechts et al., 1998; Vogel, 1994). For noninstrumented animals at low gliding speeds, other work suggests that the boundary layer remains attached up to the base of the flukes (Fish & Hui, 1991; Rohr et al., 1998). Larger tags and higher speeds may lead to short-term separation (Figure 6), though reattachment is likely, especially with active movement (Anderson, Mcgillis, &

Grosenbaugh, 2001).

Our simulations show that tag geometry and placement create a greater imbalance in these pressure fields and increase drag (Figures 6 and 7). Over the range of the simulated free-stream fluid speeds the tag increased the force acting on the modeled dolphin geometry by between 4% and 7%. The bluff elements used to increase the frontal area of the tag create large areas of fluid damming (high pressure in front of the tag), stagnate flow (low pressure) behind the tag and flow separation. These elements also create large areas of recirculating flow behind the tag perturbing the fluid flow around the animal. The additional elements increased the drag forces over the range free-stream speeds by between 47% and 77% for the *tag+4* condition and between 108% and 172% with the *tag+8* condition. These simulation results provide important insight into the effects of the tag on the coupled system, but the mechanics of the fluid in the simulations are complex, necessitating the experimental verification of the simulated results.

Glide speeds during the experimental trials (0.45–1.1 m/s) were slower than routine animal swimming speeds, translating to Reynolds numbers between 1×10^6 and 4×10^6. The animals self-selected their gliding posture, making the experimental trials more dynamic than the simulated results (Harris, 1937; Webb, 1975). Data were only used from glides selected with the protocol described in the methods, reducing the effect of body and fin movement on the experimental estimates of drag coefficients. As drag was added to the animals, variability in estimated drag coefficient increased and glide success was reduced (Figure 5). In general, animal performance of the gliding task deteriorated beyond the *tag+4* condition, with one animal unable to complete the *tag+8* condition successfully. These observations during the experiment agree with the concerns from previous work showing behavioral changes with instrumentation (Broell, Burnell, & Taggart, 2016; van der Hoop et al. 2014, 2018), and especially with large tags (Littnan, Baker, Parrish, & Marshall, 2004; Maresh et al., 2014; McMahon, Field, Bradshaw, White, &

Hindell, 2008; Solsona Berga, Wright, Galatius, Sveegaard, & Teilmann, 2015; Wilson, Grant, & Duffy, 1986). Despite the challenges associated with data collection from live animals, the experimental results show the trend predicted by simulations (Figure 7). During the experimental trials the drag elements created a large increase in drag acting on the animal, with the *tag+8* condition increasing the drag coefficient of the coupled system by 77%.

To provide context for the results presented here, both the experimental and the simulation coefficients are plotted together with other measurements and estimates found in the literature (Figure 8). Drag coefficients in our study were calculated at lower Reynolds numbers than other experimentally derived coefficients, but the control condition is comparable to drag coefficients calculated for the slow swimming speeds presented by Fish et al. (2014; teal circles). Our results are lower than Fish et al. (2014) but are for gliding, where as those in Fish et al. (2014) are for slow swimming

animals. The experimental results are plotted with ellipses that represent the uncertainty in our estimate of the coefficient and the variability of the animal's speed during the trial. The results derived from the CFD are lower than the experimental coefficients, but the control, *tag+4* and *tag+8* values fall within the uncertainty of our experimental results. We also compared the relative increase in drag created by the tag configurations from both the simulated and experimental results (Figure 7). These results are mixed, with a comparable relative increase for the *tag+4* (+47% simulation vs. +66% experiment) and *tag+8* (+108% simulation vs. +77% experiment), but not as well for the *tag* condition (+4% simulation vs. +33% experiment). The mixed results could be explained by differences between the modeled and actual dolphin geometry, self-selected gliding posture or in the orientation of the control surfaces (pectoral fins).

For both the simulation and experimental results, the bluff elements created a significant amount of added drag to the animal, but only increased the wetted surface

area of the animal by ~3% (*tag+4*) and ~5% (*tag+8*) and the frontal area of the combined system by ~9% (*tag+4*) and ~17% (*tag+8*). These results speak to benefits of tags design with hydrodynamic fairings, even if those tag designs have slightly larger surface areas or cross-sections (Shorter et al., 2014; Fiore et al., 2017). The experimental results have variability and measurement noise, but we expect our ability to estimate parameters from these data to improve as the number of experimental trials grows. As presented in Table 3, when a higher number of trials were used for the experimental estimate (e.g., *tag+4* (TT01), *no-tag* (TT01)), error bounds on were smaller. Along these lines, we had comparable agreement between the relative increase in drag at the *tag+4* condition, where we had the most data to estimate the drag coefficient (11 trials).

4.1| Limitations of the methods

More kinematic data from additional animals would improve the parameter estimates, and reduce the variability seen in the experimental results. However, there are a limited

number of facilities with animals capable of successfully performing controlled swimming tasks, resulting in a constraint on the amount of data that can be readily collected for studies like these. This makes methods that combine experimental and computation approaches appealing when investigating these types of questions. For example, the experimentally estimated drag coefficients presented here were calculated from relatively slow glides compared to average animal swimming speeds reported in the literature (0.8 m/s vs. 2 m/s), but there was no restriction on the speeds that could be investigated in simulation. Using the available experimental data to verify and improve the computational estimates will be key to improving the viability of future computational work.

In this work, differences were observed between the simulated and experimental results at the slow gliding speeds (~1 m/s). The simulated and experimental drag coefficients were within the 90% confidence interval calculated for the experimental estimates for all but the tag condition, but the results could be improved by working to

refine the animal geometry used in the modeling. Animal-specific scans could be used in both the CFD simulations and the force models used with the experimental data to produce individualized models for better comparison between methods.

While the drag estimates presented here only required planar kinematic measurements from one marker, the calibration of the camera data could be refined to improve the motion measurements. We used a simplified approach based on a known distance between two markers on the body to calibrate camera data; however, a full underwater camera calibration using methods presented, e.g., in Lavest, Rives, and Lapresté (2000) or Shortis (2015) could reduce noise in the experimental data.

4.2 | Conclusions

Quantifying the forces created by transmitting and archival tags used for animal science is an essential part of reducing the impact of these instruments. Our results suggest that computational and experimental methods can be used in a complementary manner to

determine the increase in drag associated with tags. The body of work seeking to assess the impacts of tags across taxa is growing (Barron, Brawn, & Weatherhead, 2010; Broell et al., 2016; Culik, Bannasxh, & Wilson, 1994; Jones et al., 2013; van der Hoop et al., 2014, 2018), and this work provides framework that can be used to support these studies. Additionally, the computational approach used to estimate the drag and quantify the uncertainty of the estimate from the experimental data can be applied to other data sets collected from animals in both controlled and free-swimming environments.

ACKNOWLEDGMENTS

The authors give special thanks to Dolphin Quest Oahu whose dolphin interactive facility at The Kahala Hotel & Resort served as a critically important controlled research environment for this study. Thanks to Wildlife Computers for responding to inquiries about tag dimensions and design. JVDH’s thesis committee members provided additional comments that improved the manuscript.

Ethics approval

The study protocol was approved by University of Michigan Institutional Animal Care and Use Committee (Protocol #PRO00006909).

Competing interests

The authors declare that they have no competing interests.

Funding

This project was funded by the National Oceanographic Partnership Program [National Science Foundation via the Office of Naval Research N00014-11-1-0113]. JVDH was supported by an NSERC Graduate Fellowship and the European Union's Horizon 2020 research and innovation program under the Marie Skłodowska-Curie Individual Fellowship grant agreement No 706867.

Author contributions

DZ, JVDM, VP, MM, and KS developed concepts; JVDM, MM, and JRL performed fieldwork; DZ

and JVM processed and analyzed data; VP performed the computational analysis; DZ, JVDM, VP, JRL, MM, and KS wrote the manuscript. All authors edited the manuscript. All authors read and approved the final manuscript.

REFERENCES

Anderson, E. J., Mcgillis, W. R., & Grosenbaugh, M. A. (2001). The boundary layer of swimming fish. *Journal of Experimental Biology*, *204*, 81–102.

Aoki, K., Watanabe, Y. Y., Crocker, D. E., Robinson, P. W., Biuw, M., Costa, D. P., … Miller, P. J. O. (2011). Northern elephant seals adjust gliding and stroking patterns with changes in buoyancy: Validation of at-sea metrics of body density. *Journal of Experimental Biology, 214*, 2973–2987.

Balmer, B. C., Wells, R. S., Howle, L. E., Barleycorn, A. A., McLellan, W. A., Pabst, D. A., … Zolman, E. S. (2014). Advances in cetacean telemetry: A review of single pin transmitter attachment techniques on small cetaceans and development of a new

satellite linked transmitter design. *Marine Mammal Science, 30*, 656–673.

Barron, D. G., Brawn, J. D., & Weatherhead, P. J. (2010). Meta analysis of transmitter effects on avian behaviour and ecology. *Methods in Ecology and Evolution, 1*, 180-7.

Bilo, D., & Nachtigall, W. (1980). A simple method to determine drag coefficients in aquatic animals. *Journal of Experimental Biology, 87*, 357–359.

Broell, F., Burnell, & Taggart, C. C. T. (2016). Measuring abnormal movements in free-swimming fish with accelerometers: Implications for quantifying tag and parasite load. *Journal of Experimental Biology, 219*, 695–705.

Culik, B. M., Bannasch, R., & Wilson, R. P. (1994). External devices on penguins: How important is shape? *Marine Biology, 118*, 353–357.

DiCiccio, T. J., & Efron, B. (1996). Bootstrap confidence intervals. *Statistical Science, 11*, 189–212.

Feldkamp, S. D. (1987). Swimming in the California sea lion: Morphometrics, drag and

energetics. *Journal of Experimental Biology*, 131, 117–135.

Fish, F. E. (1993). Power output and propulsive efficiency of swimming bottlenose dolphins (*Tursiops truncatus*). *Journal of Experimental Biology, 185*, 179–193.

Fish, F. E. (1998). Comparative kinematics and hydrodynamics of odontocete cetaceans: Morphological and ecological correlates with swimming performance. *Journal of Experimental Biology, 201*, 2867–2877.

Fish, F. E., & Hui, C. A. (1991). Dolphin swimming–a review. *Mammal Review, 21*, 181–195.

Fish, F. E., Legac, P., Williams, T. M., & Wei. T. (2014). Measurement of hydrodynamic force generation by swimming dolphins using bubble DPIV. *Journal of Experimental Biology, 217*, 252–260.

Fiore, G., Anderson, E., Garborg, C. S., Murray, M., Johnson, M., Moore, M. J., … Shorter, K. A. (2017). From the track to the ocean: Using flow control to improve marine bio-logging tags for cetaceans. *PloS ONE, 12*, e0170962.

Gabaldon, J., Zhang, F., Barton, K., Johnson-Roberson, M., & Shorter, K. A. (2017). A framework for enhanced localization of marine mammals using auto-detected video and wearable sensor data fusion. *IEEE/RSJ International Conference on Intelligent Robots and Systems (IROS)*, Vancouver, BC, Canada, pp. 2505–2510.

Hanson, M. B. (2001). *An evaluation of the relationship between small cetacean tag design and attachment durations: A bioengineering approach* (Doctoral dissertation). University of Washington, Seattle, WA.

Harris, J. E. (1937). *The mechanical significance of the position and movements of the paired fins in the Teleostei*. Washington, DC: Carnegie Institution of Washington.

Hazekamp, A. A., Mayer, R., & Osinga, N. (2010). Flow simulation along a seal: The impact of an external device. *European Journal of Wildlife Research, 56*, 131–140.

Hertel, H. (1966). *Structure form and movement*. New York, NY: Reinhold.

Hussey, N. E., Kessel, S. T., Aarestrup, K., Cooke, S. J., Cowley, P. D., Fisk, A. T., …

Whoriskey, F. G. (2015). Aquatic animal telemetry: A panoramic window into the underwater world. *Science, 348*, 1255642.

Irvine, A. B., Wells, R. S., & Scott, M. D. (1982) An evaluation of techniques for tagging small odontocete cetaceans. *Fishery Bulletin, 80*, 135–143.

Johnson, M., Tyack, P., Nowacek, D., & Shorter, A. (2000). A digital acoustic recording tag for measuring the response of marine mammals to sound. *Journal of the Acoustical Society of America, 108*, 2582–2583.

Jones, T., Van Houtan, K. S., Bostrom, B. L., Ostafichuk, P., Mikkelsen, J., Tezcan, E., … Seminoff, J. A. (2013). Calculating the ecological impacts of animal borne instruments on aquatic organisms. *Methods in Ecology and Evolution, 4*, 1178–1186.

Joung, T.-H., Sammut, K., He, F., & Lee, S.-K. (2012). Shape optimization of an autonomous underwater vehicle with a ducted propeller using computational fluid dynamics analysis. *International Journal of Naval Architecture and Ocean*

Engineering, 4, 44–56.

Kays, R., Crofoot, M. C., Jetz, W., & Wikelski, M. (2015). Terrestrial animal tracking as an eye on life and planet. *Science, 348*, aaa2478.

Lang, T. G., & Daybell, D. A. (1963). *Porpoise performance tests in a sea-water tank*. China Lake, CA: Naval Ordnance Test Station.

Lavest, J. M., Rives, G., & Lapresté, J. T. (2000). Underwater camera calibration. In D. Vernon (Ed.). Computer Vision — ECCV 2000. *Lecture Notes in Computer Science, Vol. 1843. Calibration/Medical Image Understanding/Visual Motion* (pp. 654–668). doi: 10.1007/3-540-45053-X

Littnan, C. L., Baker, J. D., Parrish, F. A., & Marshall, G. J. (2004). Effects of video camera attachment on the foraging behavior of immature Hawaiian monk seals. *Marine Mammal Science, 20*, 345–352.

Lockyer, C., & Morris, R. (1987). Observations on diving behaviour and swimming speeds in

a wild juvenile *Tursiops truncatus*. *Aquatic Mammals, 13*, 31–35.

López, L. M., de Soto, N. A., Miller, P., & Johnson, M. (2016). Tracking the kinematics of caudal-oscillatory swimming: A comparison of two on-animal sensing methods. *Journal of Experimental Biology, 219*, 2103–2109.

Maresh, J. L., Simmons, S. E., Crocker, D. E., McDonald, B. I., Williams, T. M., & Costa, C. P. (2014). Free-swimming northern elephant seals have low field metabolic rates that are sensitive to an increased cost of transport. *Journal of Experimental Biology, 217*, 1485–1495.

Mate, B. R., Rossbach, K. A., Nieukirk, S. L., Wells, R. S., Irvine, A. B., Scott, M. D., & Read, A. J. (1995). Satellite monitored movements and dive behavior of a bottlenose dolphin (*Tursiops truncatus*) in Tampa Bay, Florida. *Marine Mammal Science, 11*, 452–463.

McIntyre, T. (2014). Trends in tagging of marine mammals: A review of marine mammal

biologging studies. *African Journal of Marine Science, 36*, 409–422.

McMahon, C. R., Field, I. C., Bradshaw, C. J., White, G. C., & Hindell, M. A. (2008). Tracking and data–logging devices attached to elephant seals do not affect individual mass gain or survival. *Journal of Experimental Marine Biology and Ecology, 360*, 71–77.

Miller, P. J., Johnson, M. P., Tyack, P. L., & Terray, E. A. (2004). Swimming gaits, passive drag and buoyancy of diving sperm whales *Physeter macrocephalus*. *Journal of Experimental Biology, 207*, 1953–1967.

Noren, S. R., Redfern, J. V., & Edwards, E. F. (2011). Pregnancy is a drag: Hydrodynamics, kinematics and performance in pre-and post-parturition bottlenose dolphins (*Tursiops truncatus*). *Journal of Experimental Biology, 214*, 4151–4159.

Pavlov, V. V., & Rashad, A. M. (2012). A non-invasive dolphin telemetry tag: Computer design and numerical flow simulation. *Marine Mammal Science, 28*, E16–E27.

Phillips, A. B., Turnock, S. R., & Furlong, M. (2010). The use of computational fluid dynamics to aid cost-effective hydrodynamic design of autonomous underwater vehicles. *Proceedings of the Institution of Mechanical Engineers, 224*, 239–254.

Ridolix, V., Guinet, C., Liret, C., Creton, P. O., Steenstrup, R., & Beauplet, G. (1997). A video sonar as a new tool to study marine mammals in the wild: Measurements of dolphin swimming speed. *Marine Mammal Science, 13*, 196–206.

Rodi, W. (1991). Experience with two-layer models combining the k-epsilon model with a one-equation model near the wall. *29th Aerospace Sciences Meeting* (p. 216).

Rohr, J. J., Fish, F. E., & Gilpatrick, J. W. (2002). Maximum swim speeds of captive and free ranging delphinids: Critical analysis of extraordinary performance. *Marine Mammal Science, 18*, 1–9.

Rohr, J., Latz, M. I., Fallon, S. T., Nauen, J. C., & Hendricks, E. R. (1998). Experimental approaches towards interpreting dolphin-stimulated bioluminescence.

Journal of Experimental Biology, 201, 1447–1460.

Shane, S. H. (1990). Behavior and ecology of the bottlenose dolphin at Sanibel Island, Florida. In S. Leatherwood & R. R. Reeves (Eds.). *The bottlenose dolphin* (pp. 245–266). San Diego, CA: Academic Press Inc.

Shereena, S. G., Vengadesan, S., Idichandy, V. G., & Bhattacharyya, S. K. (2013). CFD study of drag reduction in axisymmetric underwater vehicles using air jets. E*ngineering Applications of Computational Fluid Mechanics, 7*, 193–209.

Shorter, K. A., Murray, M. M., Johnson, M., Moore, M., & Howle, L. E. (2014). Drag of suction cup tags on swimming animals: Modeling and measurement. *Marine Mammal Science, 30*, 726–746.

Shortis, M. (2015). Calibration techniques for accurate measurements by underwater camera systems. *Sensors, 15*, 30810–-30826. doi: 10.3390/s151229831

Skrovan, R. C., Williams, T. M., Berry, P. S., Moore, P. W., & Davis, R. W. (1999). The

diving physiology of bottlenose dolphins (*Tursiops truncatus*). II. Biomechanics and changes in buoyancy at depth. *Journal of Experimental Biology, 202*, 2749–2761.

Solsona Berga, A., Wright, A. J., Galatius, A., Sveegaard, A., & Teilmann, J. (2015). Do larger tag packages alter diving behavior in harbor porpoises? *Marine Mammal Science, 31*, 756–763.

Stelle, L. L., Blake, R. W., & Trites, A. W. (2000). Hydrodynamic drag in Steller sea lions (*Eumetopias jubatus*). *Journal of Experimental Biology, 203*, 1915–1923.

Ungerechts, B. E., Daly, D., & Zhu, J. P. (1998). What dolphins tell us about hydrodynamics. *Journal of Swimming Research, 13*, 1–7.

van der Hoop, J. M., Fahlman, A., Hurst, T., Rocho-Levine, J., Shorter, K. A., Petrov, V., & Moore, M. J. (2014). Bottlenose dolphins modify behavior to reduce metabolic effect of tag attachment. *Journal of Experimental Biology, 217*, 4229–4236.

van der Hoop, J. M., Fahlman, A., Shorter, K. A., Gabaldon, J. Rocho-Levine, J., Petrov,

V., & Moore, M. J. (2018). Swimming energy economy in bottlenose dolphins under variable drag loading. *Frontiers in Marine Science, 5*, 465.

Vogel, S. (1994). *Life in moving fluids: The physical biology of flow.* Princeton, NJ: Princeton University Press.

Ware C., Trites, A. W., Rosen, D. A., & Potvin, J. (2016). Averaged propulsive body acceleration (APBA) can be calculated from biologging tags that incorporate gyroscopes and accelerometers to estimate swimming speed, hydrodynamic drag and energy expenditure for Steller sea lions. *PloS ONE, 11*(6), e0157326.

Webb, P. W. (1975). Hydrodynamics and energetics of fish propulsion. *Bulletin of the Fisheries Research Boad of Canada, 190*, 33–48.

Williams, T. M., Friedl, W. A., & Haun, J. E. (1993). The physiology of bottlenose dolphins (*Tursiops truncatus*): Heart rate, metabolic rate and plasma lactate concentration during exercise. *Journal of Experimental Biology, 179*, 31–46.

Wilson, R. P., Grant, W. S., & Duffy, D. C. (1986). Recording devices on free-ranging marine animals: Does measurement affect foraging performance? *Ecology, 67*, 1091–1093.

Wilson, R. P., Shepard, E. L., & Liebsch, N. (2008). Prying into the intimate details of animal lives: Use of a daily diary on animals. *Endangered Species Research, 4*(1–2), 123–137.

Würsig, B., & Würsig, M. (1979). Behavior and ecology of the bottlenose dolphin, *Tursiops truncatus*, in the South Atlantic. *Fishery Bulletin, 77*, 399–412.

Yazdi, P., Kilian, A., & Culik, B. M. (1999). Energy expenditure of swimming bottlenose dolphins (*Tursiops truncatus*). *Marine Biology, 134*, 601–607.

Zhang D., Gabaldon, J., Lauderdale, L., Johnson-Roberson, M., Miller, L. J., Barton, K., & Shorter, K. (2019). Localization and tracking of uncontrollable underwater agents: Particle filter based fusion of on-body IMUs and stationary cameras. *ASME Dynamic*

Systems and Control Conference. IEEE International Conference on Robotics and Automation.

Zhang, D., Shorter, K., Rocho-Levine, J., van der Hoop, J., Moore, M., & Barton, K. (2018). Behavior inference from bio-logging sensors: A systematic approach for feature generation, selection and state classification. ASME. Dynamic Systems and Control Conference. 2018. Volume 2: V002T21A005. doi:10.1115.

TABLE 1 List of symbols and abbreviations.

Symbol	Definition	Unit
a	Acceleration	m/s^2
a_f	Face area (in CFD)	m^2
a_{ref}	Reference area (in CFD)	m^2
A_w	Wetted surface area	m^2
b	Index of estimated drag coefficient (in Bootstrapping)	
B	Total number of estimated drag coefficients (in Bootstrapping)	
C_d	Drag coefficient	
$C_{d\ correct}$	Drag coefficient that has surface induced drag corrected	
CAD	Computer aided design	
CFD	Computational fluid dynamics	
d_w	Distance between kinematic markers in real world	m
d_v	Distance between kinematic markers in video frame	pixel
F_d	Drag force	N
$F_f^{pressure}$	Pressure force on the surface face f (in CFD)	N
F_f^{shear}	Shear force on the surface face f (in CFD)	N
k	Index of one good trial	
K	Total number of good trials	
l	Body length	m
m_b	Induced body mass	Kg
n	Index of drag coefficient candidate in parameter sweep	
N	Total number of drag coefficient candidates	

p_f	Face static pressure (in CFD)	Pa
p_{ref}	Reference pressure (in CFD)	Pa
ρ	Density	kg/m^3
ρ_{ref}	Reference density (in CFD)	kg/m^3
R	Fitting error (cost) for one trial (in parameter sweep)	
R_{all}	Fitting error (cost) over all trials (in parameter sweep)	
Re	Reynolds number	
t	Time	s
T_f	Stress tensor at face f (in CFD)	Pa
U	Speed (in real world)	m/s
U_0	Initial speed (in real world)	m/s
U_v	Speed (in video)	pixel/s
v	Kinematic viscosity	m^2/s
v_{ref}	Reference velocity (in CFD)	m/s
γ	Drag coefficient correct factor for surface induced drag	

TABLE 2 Weight (kg) and length (m) of the two bottlenose dolphins in the study, their estimated wetted surface area (calculated from Fish, 1993) and the number of glides they each successfully performed for each experimental condition. Girth was measured approximately two fingers in front of the dorsal fin after animals exhaled.

Subject	Weight (kg)	Length (m)	Girth (m)	Frontal area (m^2)	Wetted surface area (m^2)	No tag	Tag	Tag+4	Tag+8
TT01 (63H4)	176	2.52	1.23	0.12	2.39	5	1	7	0
TT02 (01L5)	154	2.37	1.21	0.12	2.19	4	3	4	3

TABLE 3 Drag coefficients (C_d) calculated from the individual fitting to speed data, the number of successful trials, and the resulting fit residuals (R). The results from fitting to all of the data for a given trial (C_{d_all}) as well as the corresponding drag coefficient that has compensated for surface drag ($C_{d\_all\_comp}$), the 90% confidence interval are presented below.

Conditions and animals	Parameters	Trial #1	Trial #2	Trial #3	Trial #4	Trial #5	Trial #6	Trial #7	Mean	*SD*	C_{d_all}	$C_{d\_all\_correct}$

No Tag (TT01)	C_d	0.017	0.010	0.013	0.017	0.013	—	—	0.014	0.003	0.0137 ± 0.006	0.0125 ± 0.0055
	R	0.077	0.107	0.040	0.123	0.128	—	—	0.095	0.037	—	—
	R (C_{d_all})	0.077	0.107	0.040	0.123	0.128	—	—	0.095	0.037	—	—
	U_0	0.780	0.790	0.790	0.990	1.050	—	—	0.874	0.136	—	—
	Duration	1.933	1.567	0.933	0.967	1.533	—	—	1.387	0.429	—	—
Tag (TT01)	C_d	0.011	—	—	—	—	—	—	0.011	0.000	0.011 ± 0.01	0.010 ± 0.0091
	R	0.209	—	—	—	—	—	—	0.209	0.000	—	—
	R (C_{d_all})	0.209	—	—	—	—	—	—	0.209	0.000	—	—
	U_0	0.740	—	—	—	—	—	—	0.740	0.000	—	—
	Duration	3.567	—	—	—	—	—	—	3.567	0.000	—	—
Tag+4 (TT01)	C_d	0.027	0.018	0.015	0.023	0.038	0.034	0.039	0.027	0.010	0.0225 ± 0.002	0.0205 ± 0.0018
	R	0.062	0.042	0.054	0.062	0.081	0.066	0.053	0.060	0.012	—	—
	R (C_{d_all})	0.063	0.045	0.060	0.062	0.090	0.069	0.056	0.064	0.014	—	—
	U_0	0.780	1.050	1.070	1.040	1.060	0.970	0.930	0.986	0.104	—	—
	Duration	3.367	1.967	1.933	2.100	2.000	1.333	0.900	1.943	0.765	—	—
No Tag (TT02)	C_d	0.023	0.020	0.011	0.004	—	—	—	0.014	0.009	0.0158 ± 0.005	0.0121 ± 0.0038
	R	0.050	0.151	0.203	0.186	—	—	—	0.147	0.069	—	—
	R (C_{d_all})	0.052	0.151	0.204	0.190	—	—	—	0.149	0.069	—	—
	U_0	0.920	0.950	1.020	0.890	—	—	-	0.945	0.056	—	—
	Duration	1.800	2.233	2.633	1.967	—	—	-	2.158	0.364	—	—
Tag (TT02)	C_d	0.027	0.013	0.024	—	—	—	—	0.021	0.007	0.021 ± 0.005	0.0161 ± 0.0038
	R	0.055	0.025	0.200	—	—	—	—	0.093	0.094	—	—
	R (C_{d_all})	0.056	0.027	0.201	—	—	—	—	0.094	0.093	—	—
	U_0	0.720	0.650	0.980	—	—	—	—	0.783	0.174	—	—
	Duration	1.667	1.733	3.100	—	—	—	—	2.167	0.809	—	—
Tag+4 (TT02)	C_d	0.026	0.031	0.023	0.039	—	—	—	0.030	0.007	0.0265 ± 0.009	0.0203 ± 0.0069
	R	0.171	0.150	0.142	0.274	—	—	—	0.184	0.061	—	—
	R (C_{d_all})	0.171	0.151	0.142	0.274	—	—	—	0.184	0.061	—	—
	U_0	0.670	0.720	0.800	0.700	—	—	—	0.723	0.056	—	—
	Duration	2.667	2.667	2.300	1.033	—	—	—	2.167	0.775	—	—
Tag+8—(TT02)	C_d	0.033	0.023	0.037	—	—	—	—	0.031	0.007	0.028 ± 0.01	0.0214 ± 0.0077
	R	0.100	0.188	0.078	—	—	—	—	0.122	0.059	—	—

R (C_{d_all})	0.100	0.189	0.079	—	—	—	—	0.123	0.059	—	—
U_0	0.500	0.800	0.750	—	—	—	—	0.683	0.161	—	—
Duration	2.033	3.467	1.600	—	—	—	—	2.367	0.977	—	—

TABLE 4 Wetted surface area (A_w), drag coefficients (C_d), percent increase in drag coefficient, and the net drag forces (F_d) calculated from the CFD simulations at various speeds.

Condition	A_w (m^2)	F_d(N) 1 m/s	C_d	F_d (N) 2 m/s	C_d	F_d (N) 3 m/s	C_d	F_d (N) 4 m/s	C_d	F_d (N) 5 m/s	C_d	F_d (N) 6 m/s	C_d
Control	2.915	14.9	0.010	49.8	0.008	102.4	0.008	177.2	0.007	272.0	0.007	387.0	0.007
Tag	2.939	15.6	0.010	52.6	0.009	109.0	0.008	188.6	0.008	290.2	0.008	412.5	0.008
Tag+4	2.983	22.5	0.015	81.6	0.013	175.8	0.013	308.6	0.013	475.2	0.012	686.1	0.013
Tag+8	3.029	32.3	0.021	122.3	0.020	267.8	0.019	472.2	0.019	734.5	0.019	1053.8	0.019

FIGURE 1 Illustration of the experiment (A) conducted to collect kinematic data during different drag loading conditions (B and C): *control*, *tag*, *tag+4* and *tag+8*. A: Zinc oxide applied to the dolphin's skin was used to create the kinematic markers. Planar video data of the animals during gliding were collected using an underwater camera. B: the modular system including the tag and drag elements, built to increase drag loading on the animals. C: expected net drag in the different drag loading conditions.

FIGURE 2 (a) Example video frame of a gliding dolphin with kinematic markers (zinc oxide) under the dorsal fin. (b) Preprocessing was used to enhance the visibility of the markers for automatic tracking of the data. (c) Tracked kinematic markers with the identified features are visualized with red circles. The average feature position is shown as a black triangle. The distance (Δx) between the two fixed kinematic markers as the dolphin glides through the frame was calculated for calibration and undistortion. (d) The horizontal position of animal in the

video frame is shown on the *x*-axis. Pincushion distortion created by the lens results in as much as an 8-mm change in distance between the markers at the edges of the frame.

FIGURE 3 Representative data from a glide during the *tag* condition. (Top left) top view of the optimization surface used to select the model parameters (U_o and C_d). Parameters that minimize fit residuals are indicated by the red circle. (Top middle) RMS (root mean square) value of fitting residual versus initial speed U_0. (Top right) RMS value of fitting residual versus drag coefficient C_d. (Middle) Measured (solid black) and the corresponding dynamic model prediction of the speed using the parameters selected using optimization. (Bottom) A representative iteration of the resampling and refitting to illustrate how bootstrapping was used to create a confidence interval for the drag coefficient.

FIGURE 4 Illustration of the dolphin-tag model in the computational domain used for the simulations of all tag conditions. Velocity results from a representative simulation in 3 m/s steady state flow are presented in the

figure.

FIGURE 5 (Top) Average and individual initial velocities calculated during the parameter optimization for both animals. Error bars indicate one standard deviation around the mean value. (Bottom) Mean and individual glide duration of each successful trial. Error bars indicate one standard deviation around the mean value.

FIGURE 6 Computational fluid dynamics simulation results from the dolphin and combined dolphin-tag models that illustrate how the tag and added drag elements affect the velocity of the flow (left) and the resulting pressure differentials (right) around the model of the animal.

FIGURE 7 (Top) Net drag forces calculated from the Computational fluid dynamics simulation results. The *control* and *tag* conditions have similar net forces over the range of simulated speeds, but the additional of the drag elements greatly increases the force acting on the combined body. The yellow circle highlights the results near 1 m/s, a comparable speed to the gliding trials. (Bottom) A comparison of the estimated drag force acting

on TT02 at speed of 1 m/s during the four experimental conditions over simulation (Sim) and experiment results that have been corrected for surface drag effect (Exp Cor) as well as the uncorrected raw drag force (Exp Uncor). The percent increase over the respective control trial is provided for all of the tagged conditions. The 90% confidence interval is also plotted with the experimental data.

FIGURE 8 Drag coefficients of dolphins from historical data compared to this study. Data from this study follow the same convention as our other figures (black circles = *no tag*; blue triangles = *tag*; green diamonds = *tag+4*; red squares = *tag+8*). The uncertainty ellipse around each of the experimentally derived drag coefficients was formed using the 90% confidence bound calculated using bootstrapping and the standard deviation of the initial velocity data. Unfilled symbols represent results from Computational fluid dynamics. Results from this work are shown alongside data from the literature as presented in Fish et al. (2014). Experiments on rigid models, towed

bodies and gliding animals (maroon circles), from hydrodynamic models based on swimming kinematics (orange circles), from a rigid “dolphin” model with the shape of a solid of revolution of the NACA 66 series (yellow circles), and from particle image velocimetry (teal circles). As in Fish (2014), the black line represents the frictional drag coefficient for a flat plate with turbulent boundary layer flow and the dashed line is for a flat plate with laminar boundary flow.

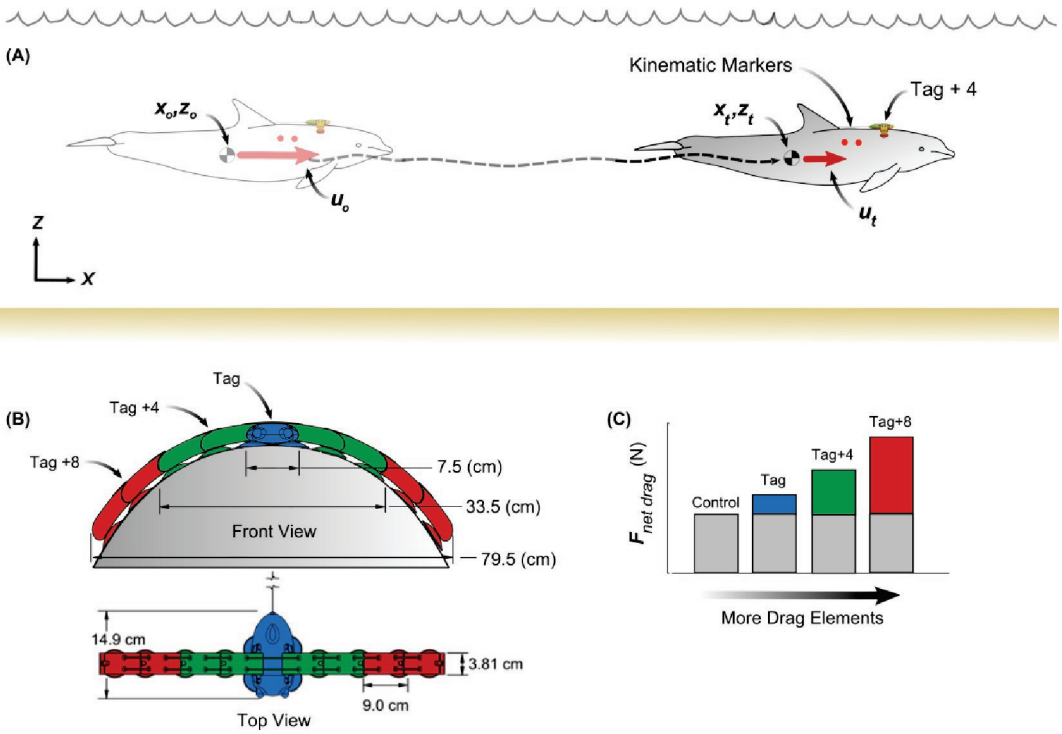

mms_12627_4664_fig1.eps

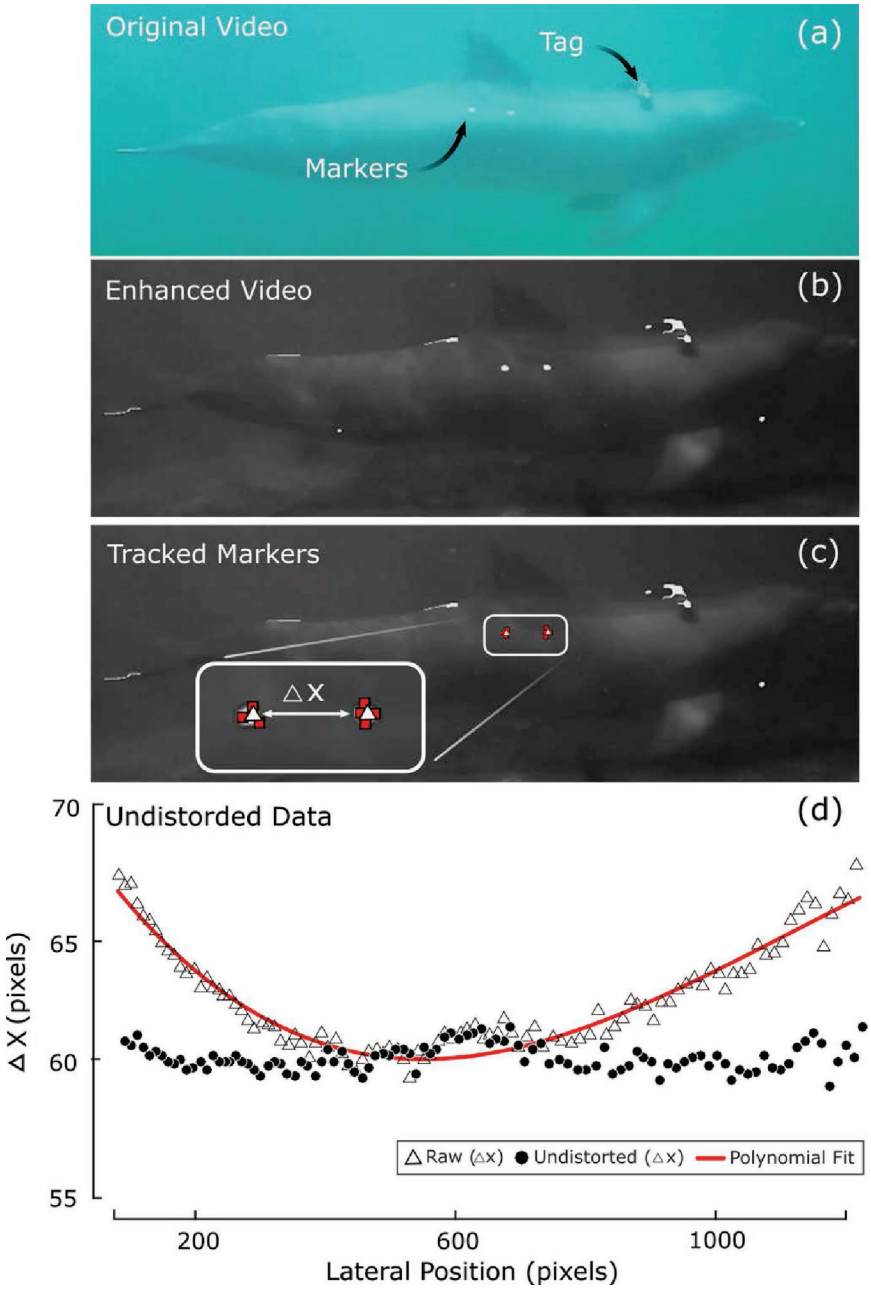

mms_12627_4664_fig2.eps

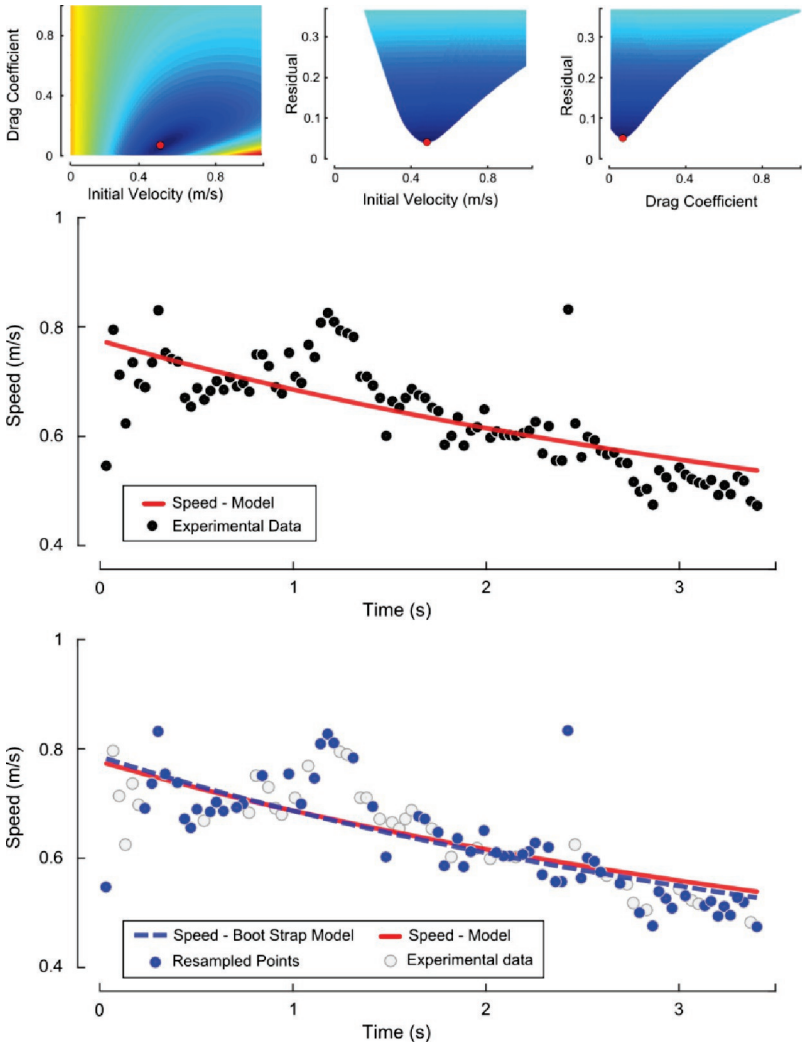

mms_12627_4664_fig3.eps

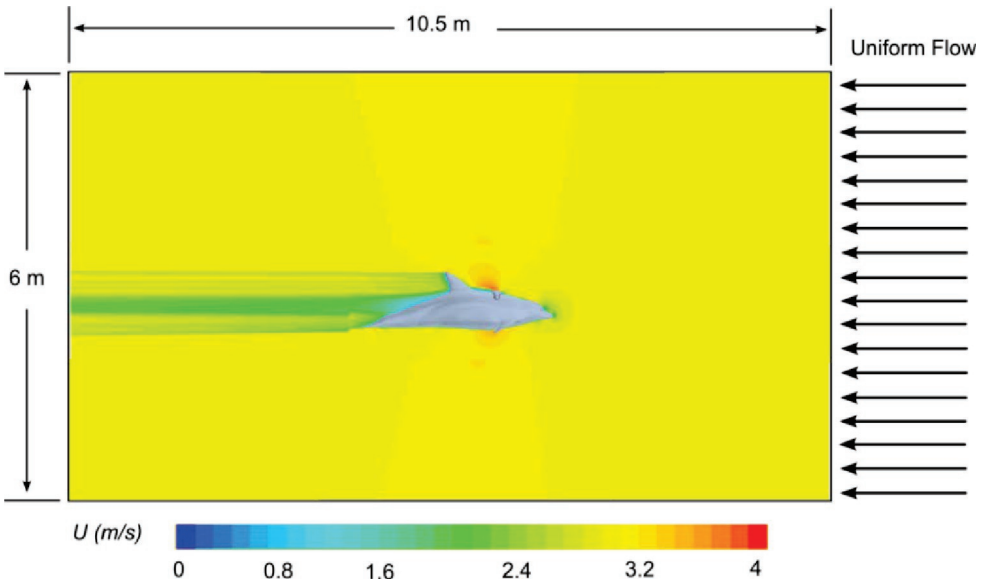

mms_12627_4664_fig4.eps

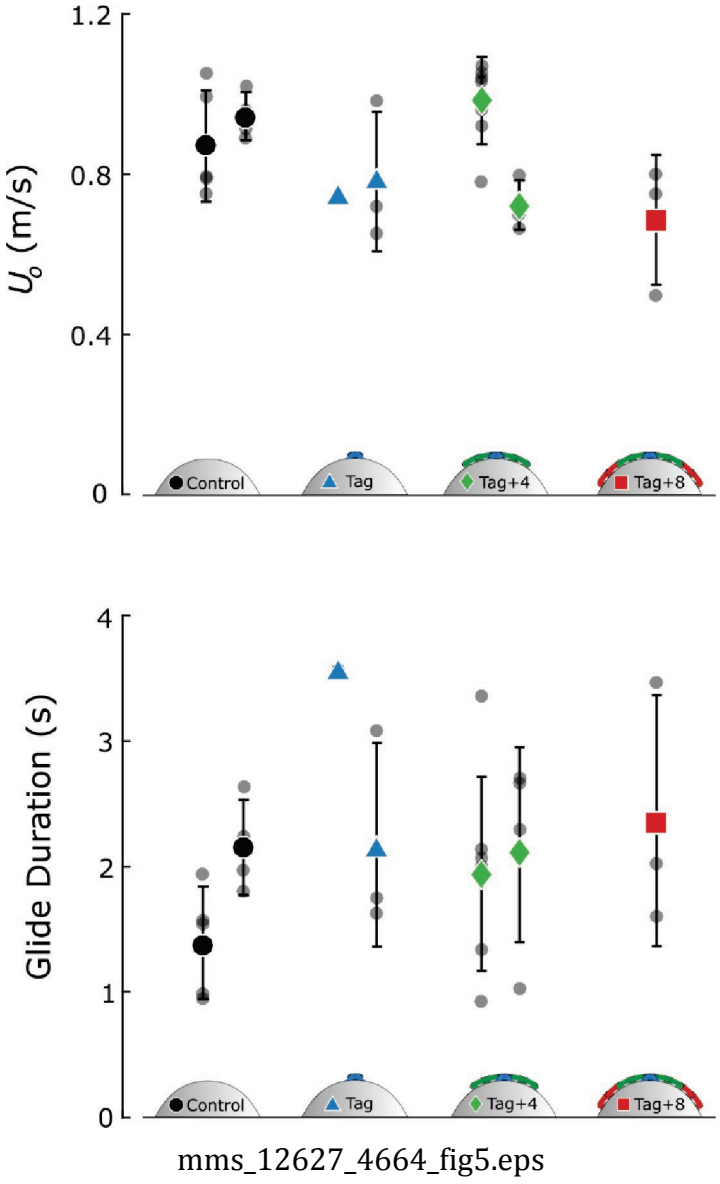

mms_12627_4664_fig5.eps

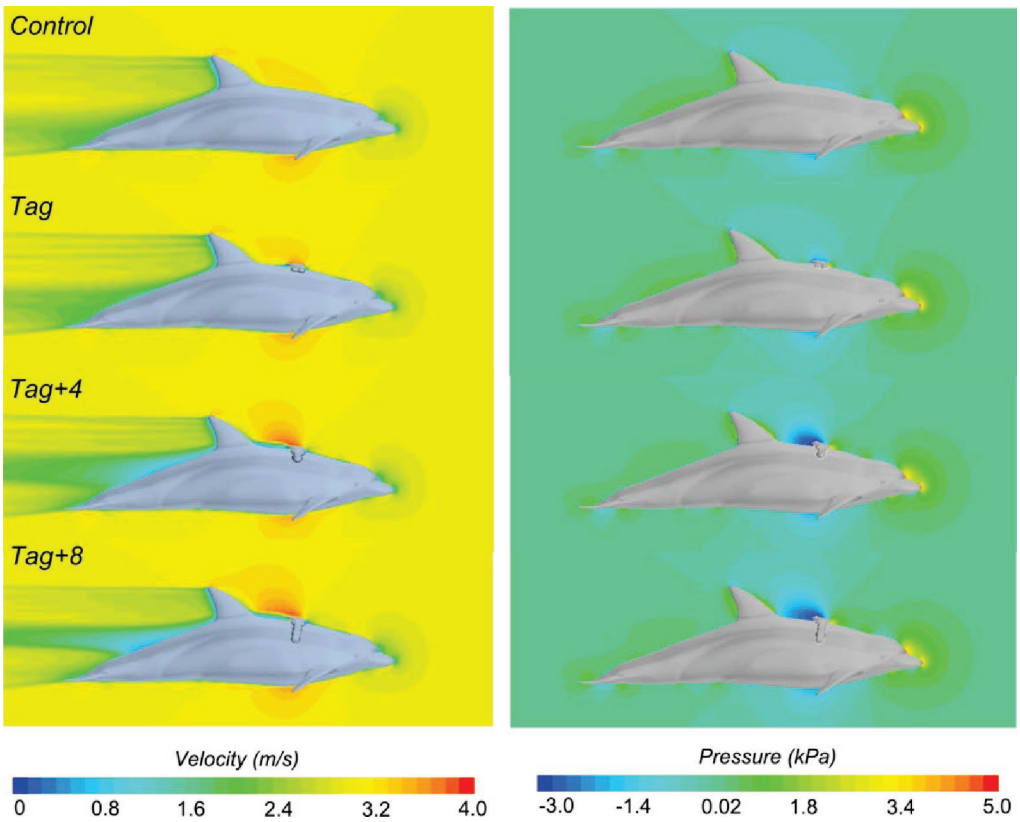

mms_12627_4664_fig6.eps

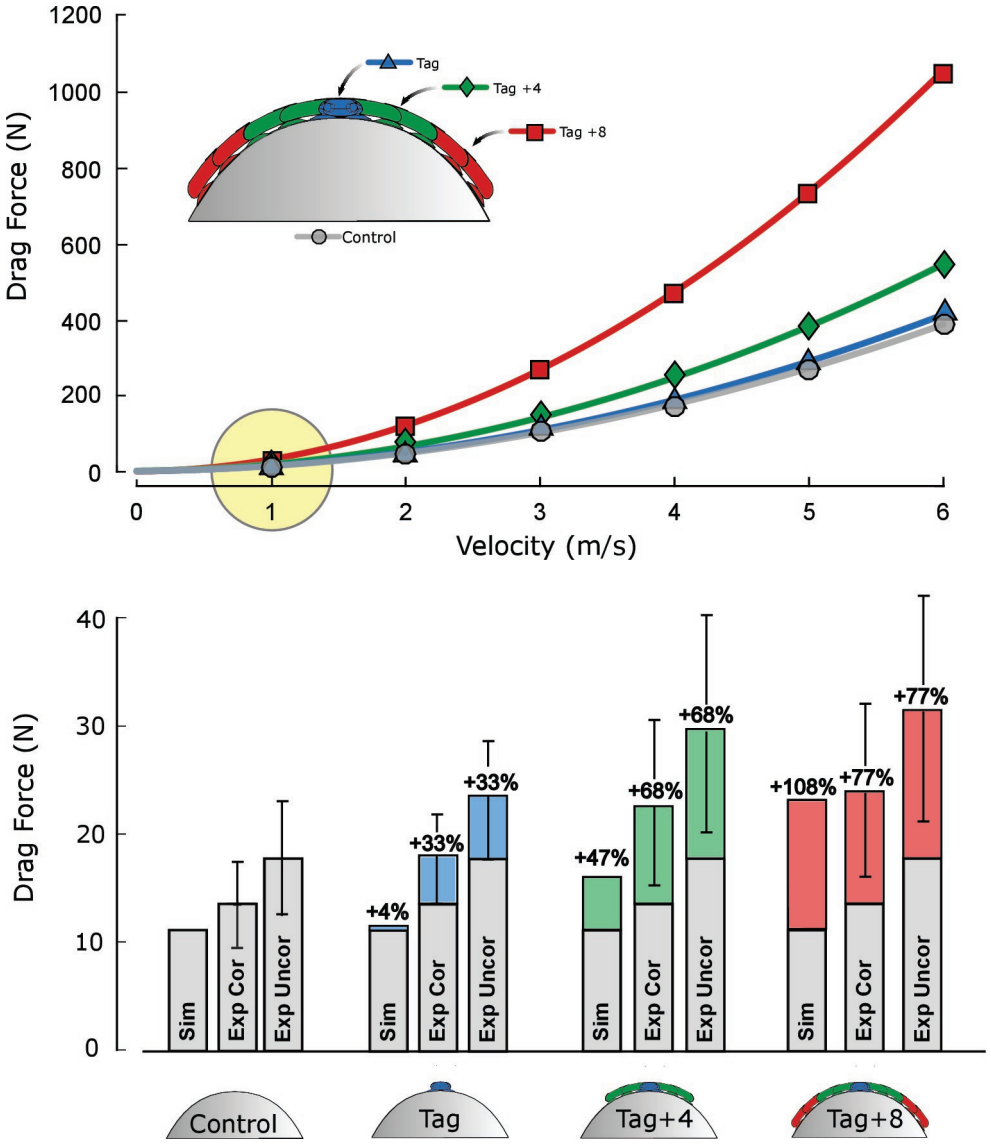

mms_12627_4664_fig7.eps

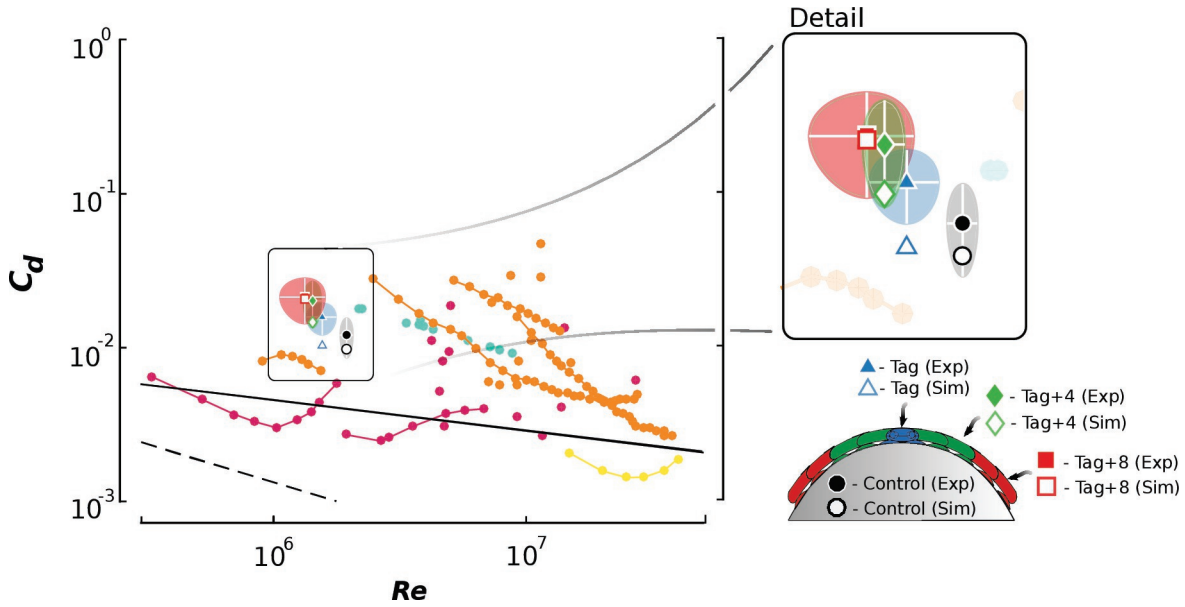

mms_12627_4664_fig8.eps